Electronic supplementary information

Anchoring porous carbon nanoparticles on carbon nanotubes as high-performance composite with a unique core-sheath structure for electromagnetic pollution precaution

Honghong, Zhao, Xianzhu Xu*, Dingge Fan, Ping Xu, Fengyuan Wang, Liru Cui, Xijiang Han*, and Yunchen Du*

MIIT Key Laboratory of Critical Materials Technology for New Energy Conversion and Storage, School of Chemistry and Chemical Engineering, Harbin Institute of Technology, Harbin 150001, P.R. China

---

** Corresponding authors.*

yunchendu@hit.edu.cn (Y. Du); hanxijiang@hit.edu.cn (X. Han); xuxianzhu@hit.edu.cn (X. Xu).

Tel: +86-(451)-86418750; fax: +86-(451)-86413702.

Material Characterization

Scanning electron microscope (SEM, HELIOS NanoLab 600i) was used to collect the SEM images for observing morphology of the samples, and the operating voltage is 20 kV. Powder X-ray diffraction (XRD) data were recorded on a Rigaku D/MAXRC X-ray diffractometer with Cu Ka radiation source (45.0 kV, 50.0 mA). X-ray photoelectron spectra (XPS) were obtained with PHI 5700 ESCA system equipped with an A1 K radiation as a source (1486.6 eV). Raman spectra were performed on a confocal Raman spectroscopic system (Renishaw, In Via) using a 532 nm laser. Transmission electron microscope (TEM, JEOL JEM-3000F) was utilized to collect the TEM images for observing configuration of the samples, and the operating voltage is 200 kV. Thermogravimetric (TG) analysis was determined on SDT Q600 TGA (TA Instruments) within a temperature range of room temperature to 800 °C with a heating rate of 10 °C/min under air atmosphere. A four-probe resistivity meter (RTS-9, Guangzhou 4-probes Technology Co., Ltd, China) was utilized to measure the electronic conductivity of these samples. Nitrogen adsorption isotherms were measured at 196 °C on a QUADRASORB SI-KR/MP (Quantachrome, USA). Samples were normally synthesized for measurement by degassing at 120 °C. We used an Agilent N5234A vector network analyzer (Agilent, USA) to obtain the relative permeability and permittivity in the frequency range of 2.0-18.0 GHz for the calculation of reflection loss. A sample containing 10 wt% of the as-prepared product was pressed into a ring with a thickness of 2 mm, an outer diameter of 7 mm, and an inner diameter of 3 mm for microwave measurement in which paraffin wax was applied as the binder.

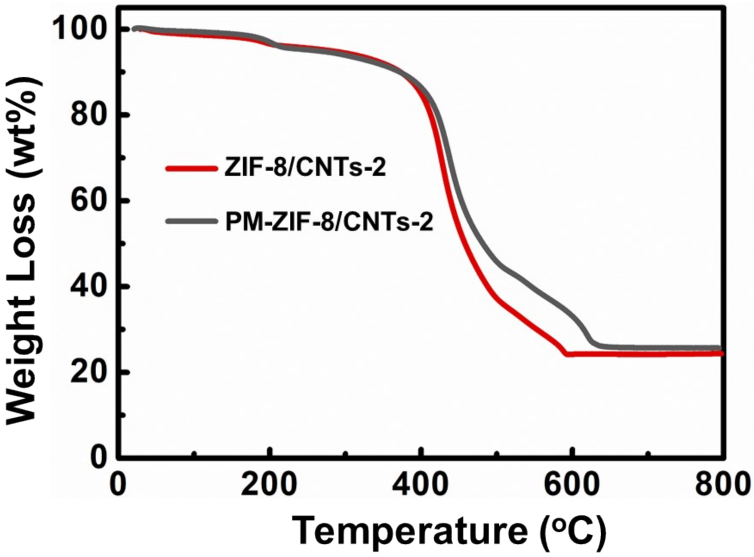

Fig. S1 TG curves of ZIF-8/CNTs-2 and PM-ZIF-8/CNTs-2.

The content of ZIF-8 in ZIF-8/CNTs-2 and PM-ZIF-8/CNTs-2 can be calculated from the following equation:

$$wt\%R = (wt\%\ ZIF-8)\frac{M(ZnO)}{M(ZIF-8)} \tag{1}$$

where wt% R is the remaining weight percentage after combustion, and M refers to the molecular weights of ZnO and ZIF-8.

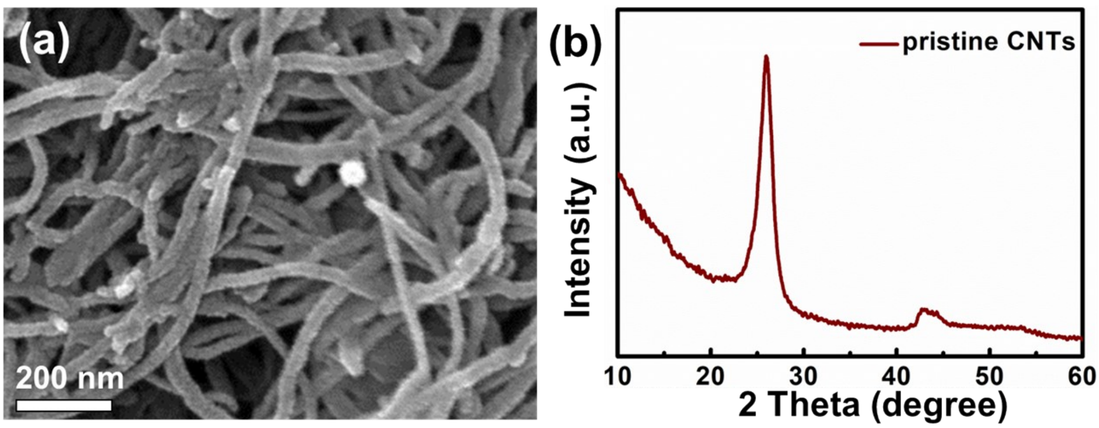

Fig. S2 SEM image (a) and XRD pattern (b) of pristine CNTs.

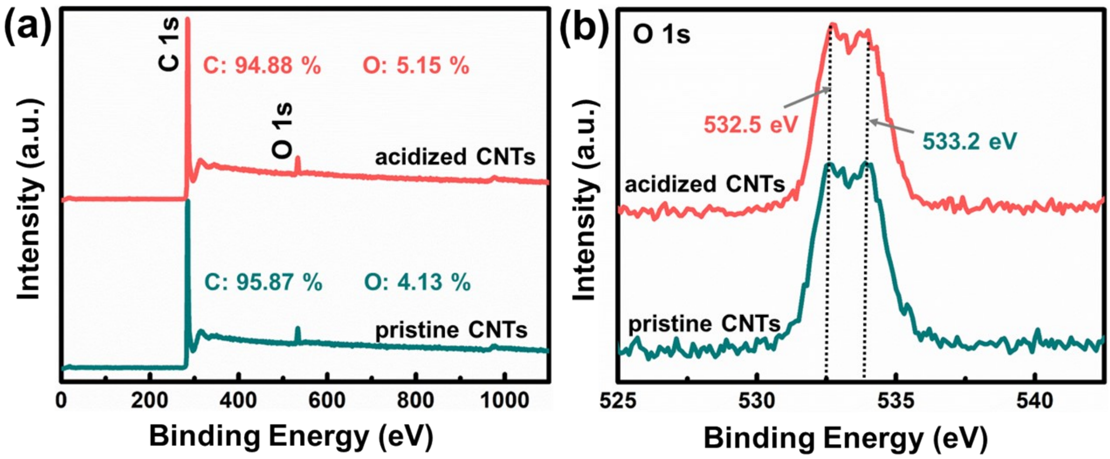

Fig. S3 XPS survey (a) and spectra of O1s (b) for pristine CNTs and acidized CNTs.

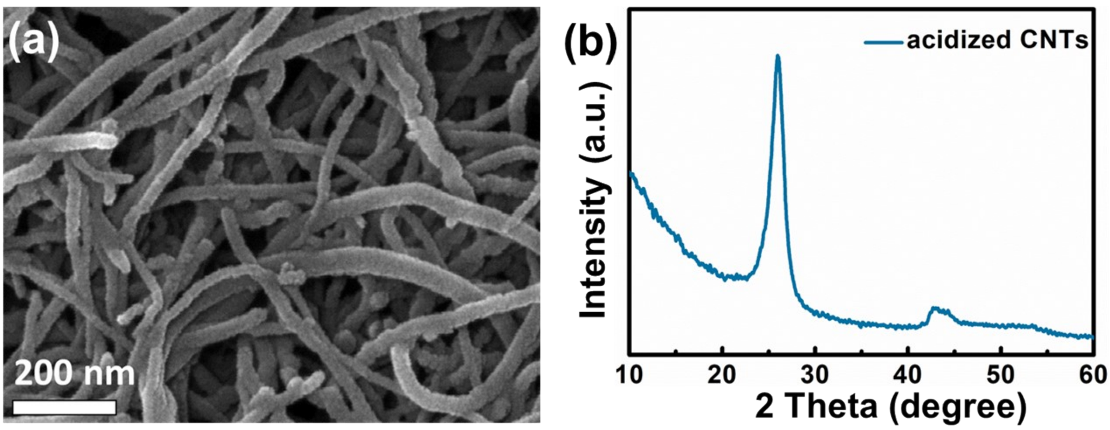

Fig. S4 SEM image (a) and XRD pattern (b) of acidized CNTs.

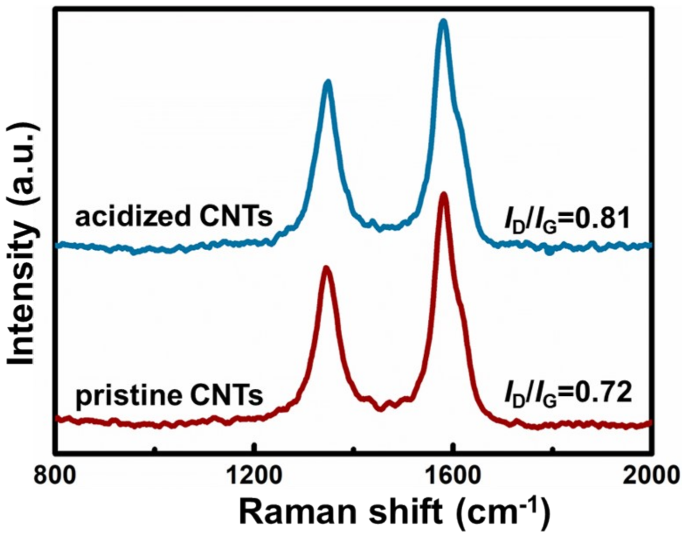

Fig. S5 Raman spectra of pristine CNTs and acidized CNTs.

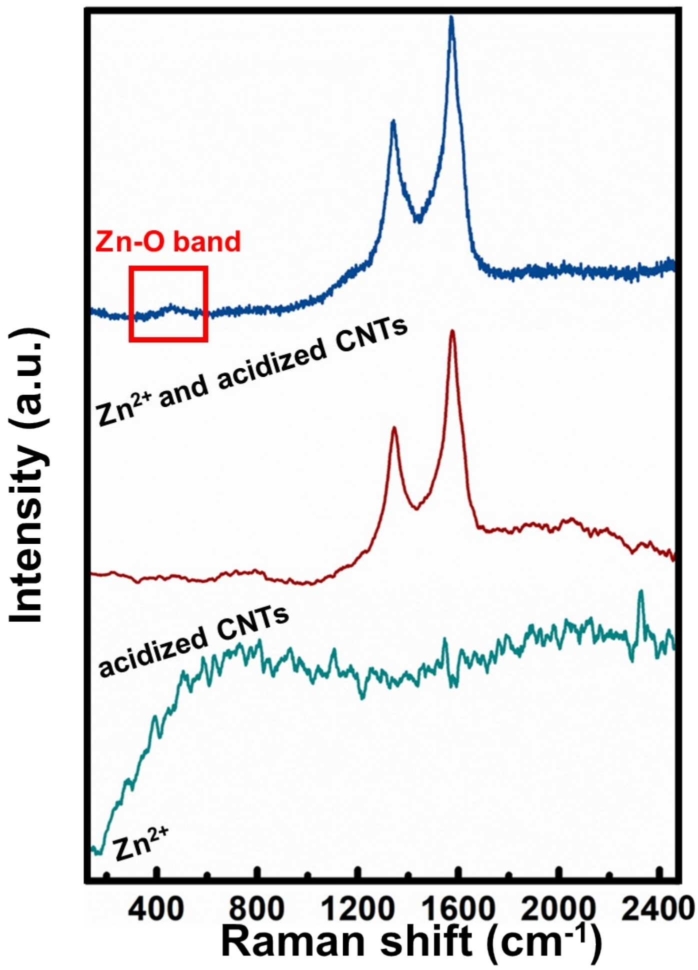

Fig. S6 Raman spectra of individual Zn^{2+} solution, acidized CNTs, and Zn^{2+}/acidized CNTs.

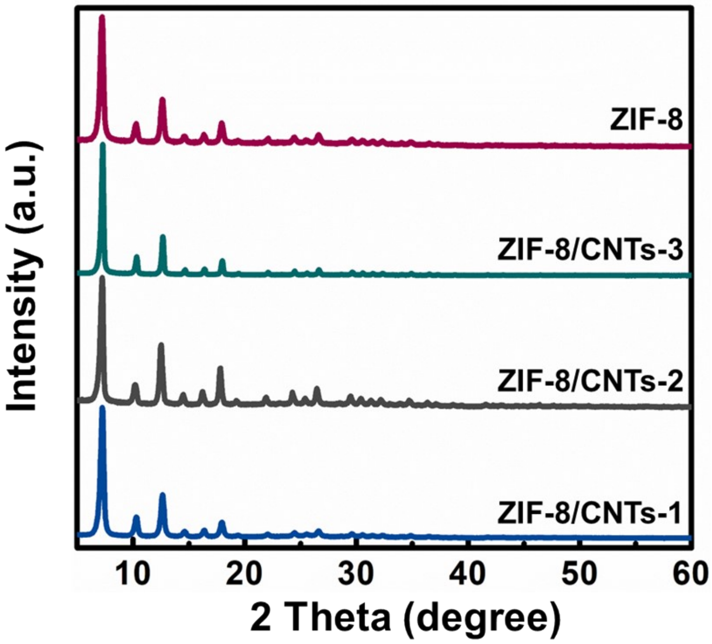

Fig. S7 XRD patterns of ZIF-8/CNTs-1, ZIF-8/CNTs-2, ZIF-8/CNTs-3 and ZIF-8.

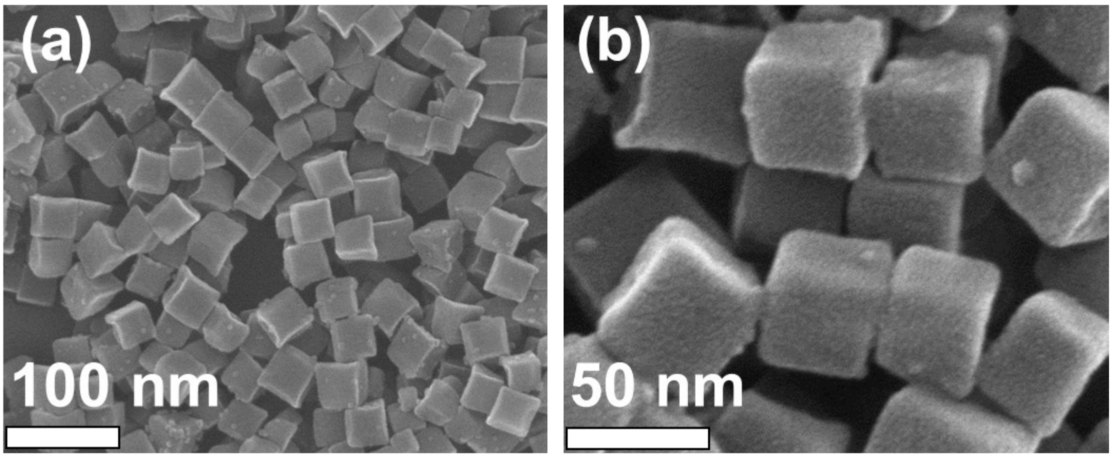

Fig. S8 SEM images of ZIF-8 nanocubes.

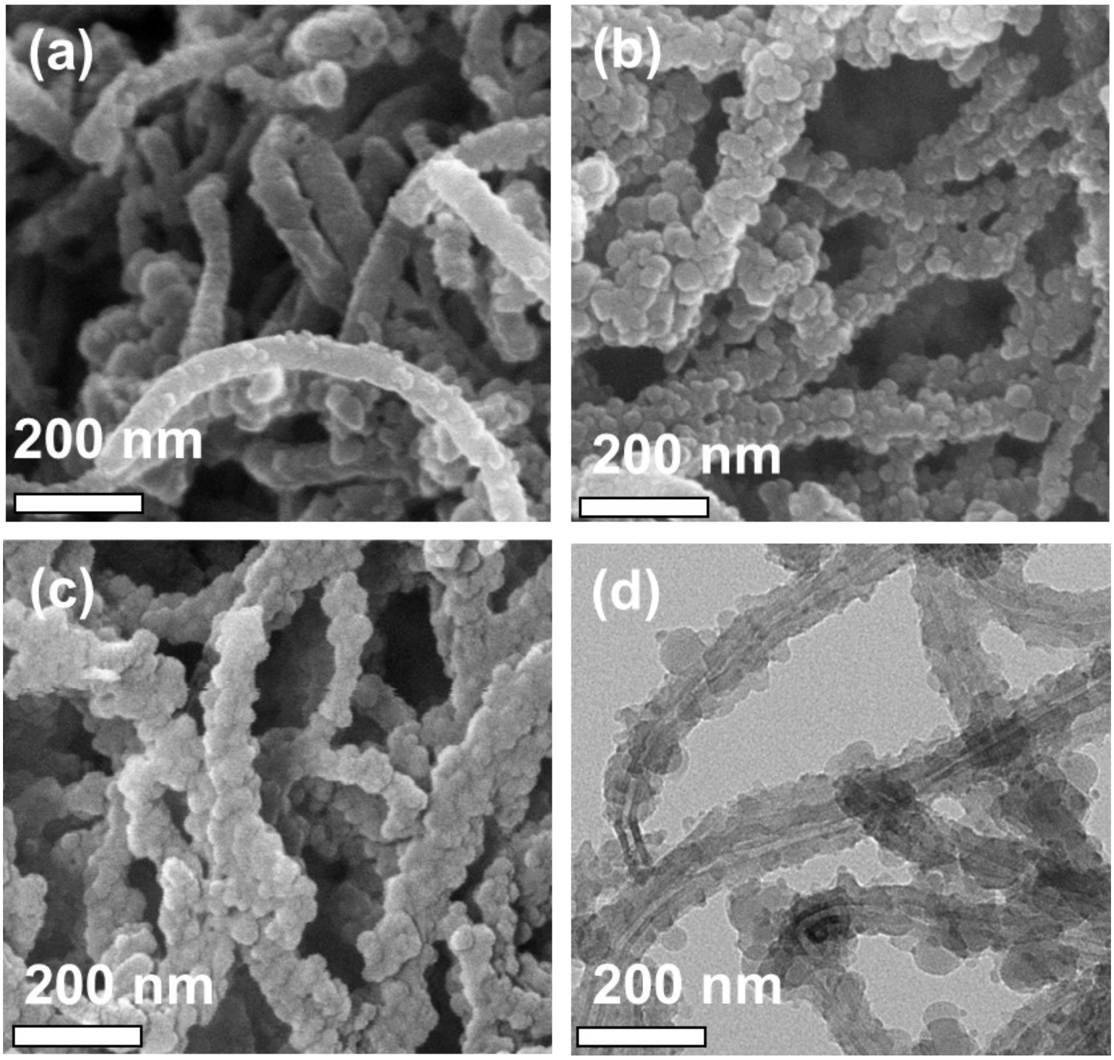

Fig. S9 SEM images of ZIF-8/CNTs-1 (a), ZIF-8/CNTs-2 (b), ZIF-8/CNTs-3 (c), and TEM image of ZIF-8/CNTs-2 (d).

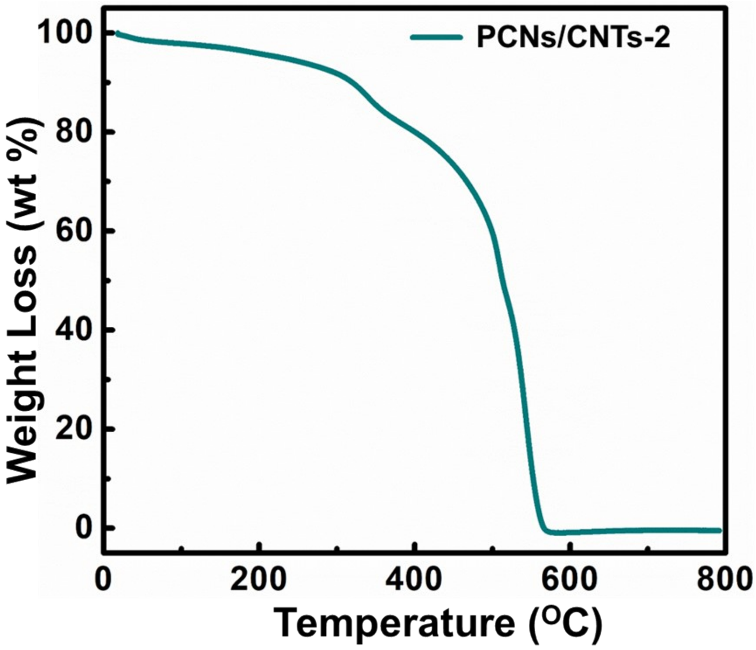

Fig. S10 TG curve of PCNs/CNTs-2.

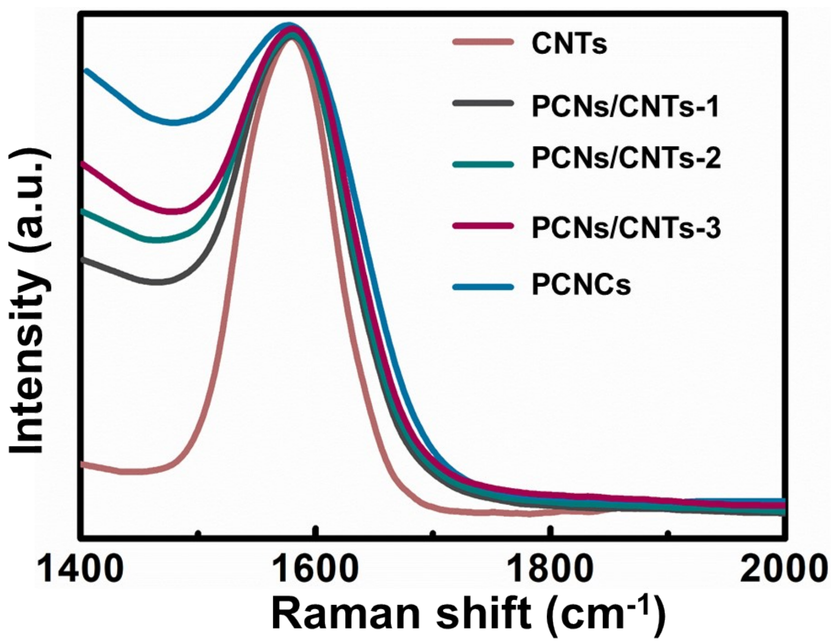

Fig. S11 The local magnification of G bands in Raman spectra for CNTs, PCNs/CNTs-1, PCNs/CNTs-2, PCNs/CNTs-3, and PCNCs.

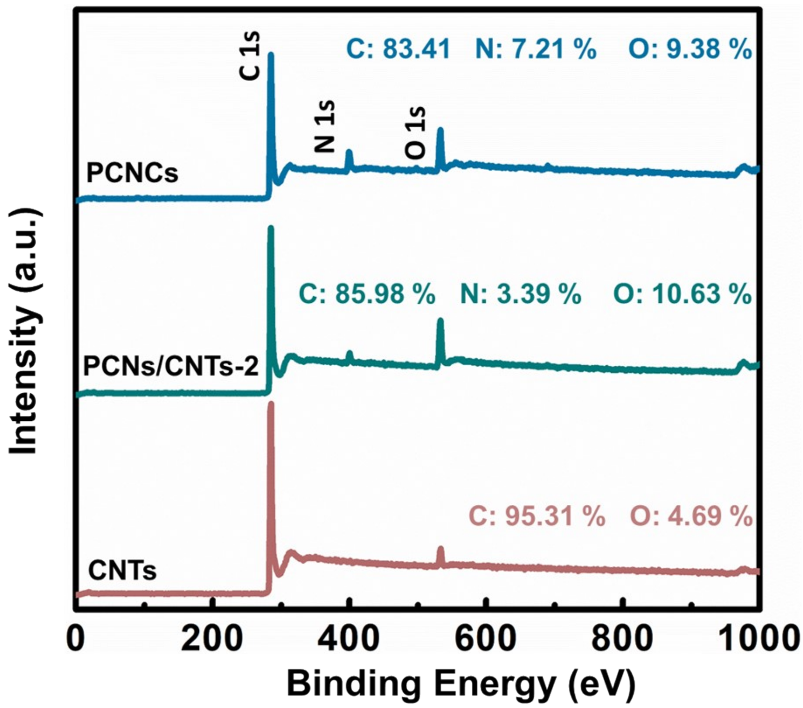

Fig. S12 XPS survey of CNTs, PCNs/CNTs-2 and PCNCs.

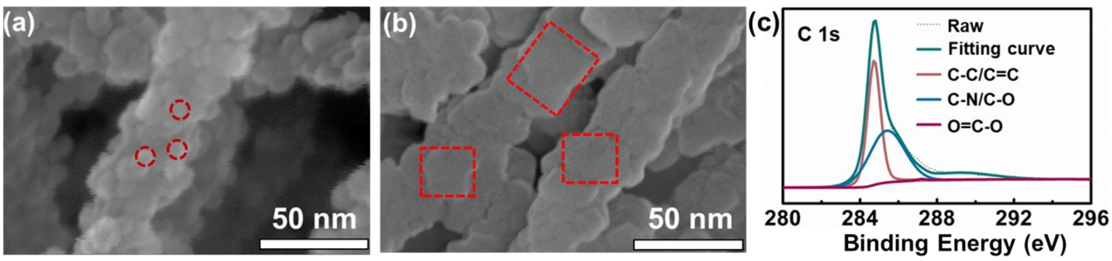

Fig. S13 High-magnification SEM images of PCNs/CNTs -2 (a) and PCNs/CNTs -2 (L) (b); C1s spectrum of PCNs/CNTs -2 (L) (c).

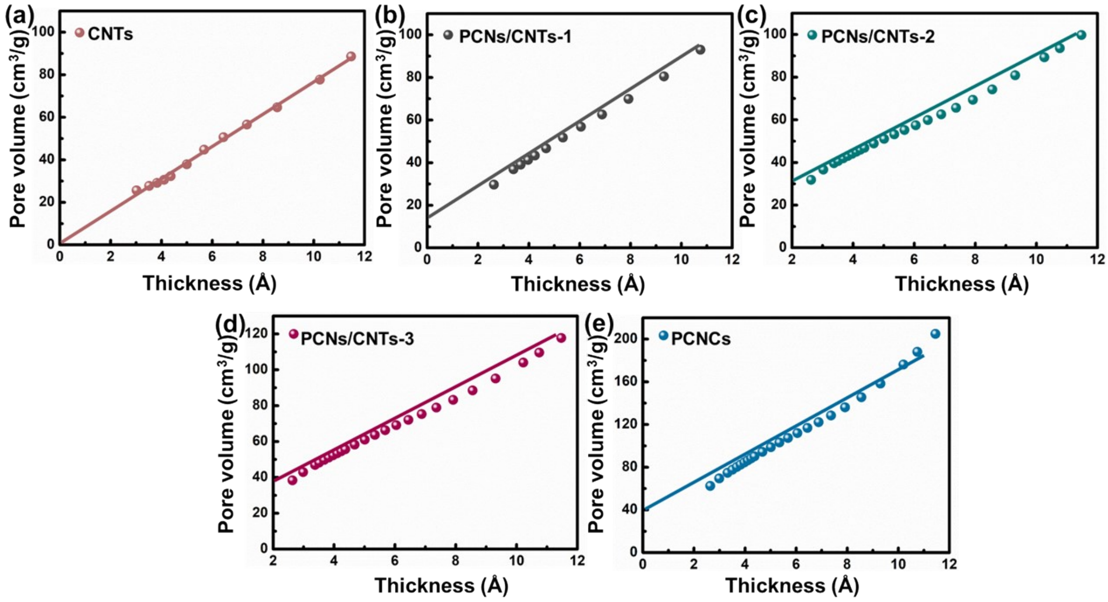

Fig. S14 *t*-plots of CNTs (a), PCNs/CNTs-1 (b), PCNs/CNTs-2 (c), PCNs/CNTs-3 (d), and PCNCs (e).

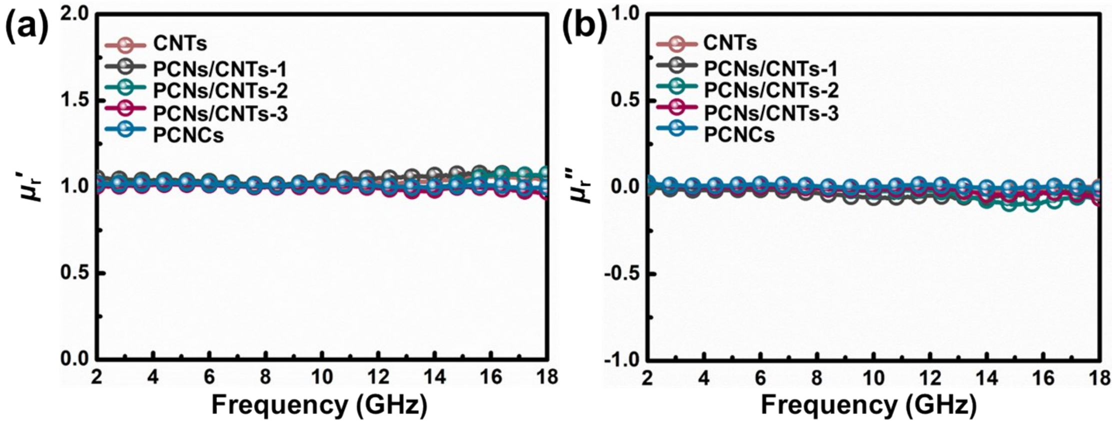

Fig. S15 Real parts (a) and imaginary parts (b) of CNTs, PCNs/CNTs-1, PCNs/CNTs-2, PCNs/CNTs-3, and PCNCs.

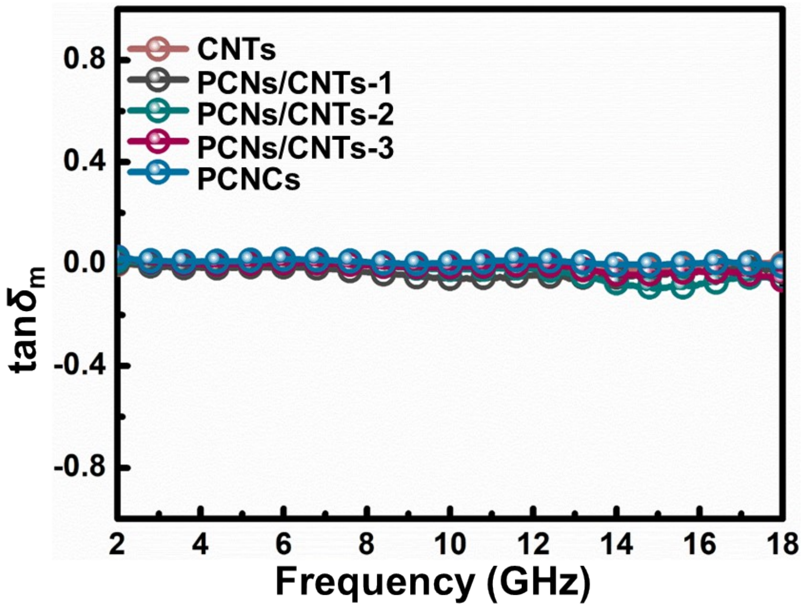

Fig. S16 Magnetic loss tangents of CNTs, PCNs/CNTs-1, PCNs/CNTs-2, PCNs/CNTs-3, and PCNCs.

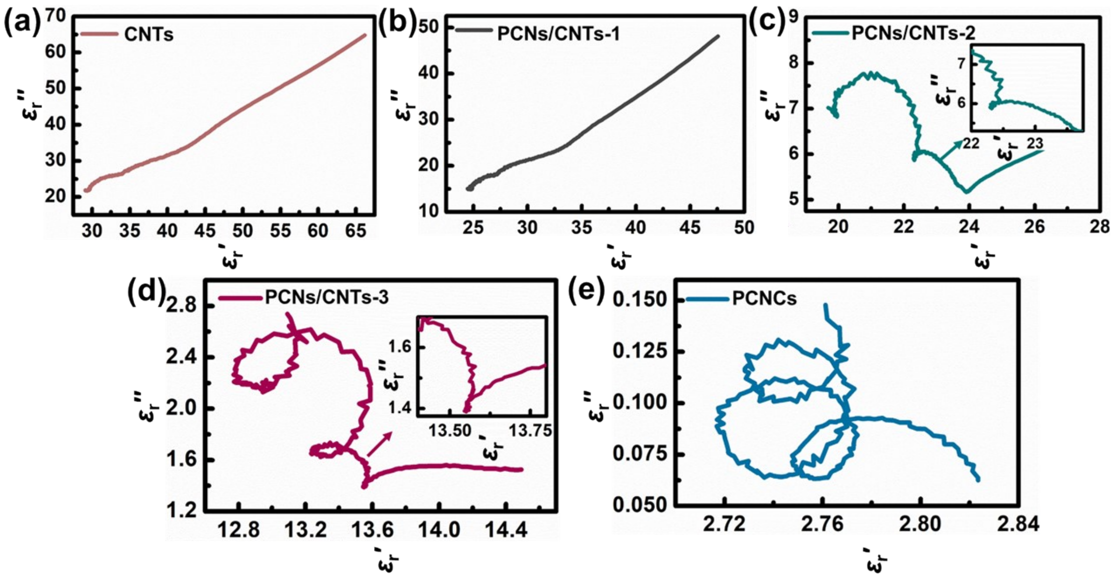

Fig. S17 Cole-Cole semicircles (ε_r''-ε_r') of CNTs (a), PCNs/CNTs-1 (b), PCNs/CNTs-2 (c), PCNs/CNTs-3 (d), PCNCs (e), respectively, in the frequency range of 2.0-18.0 GHz.

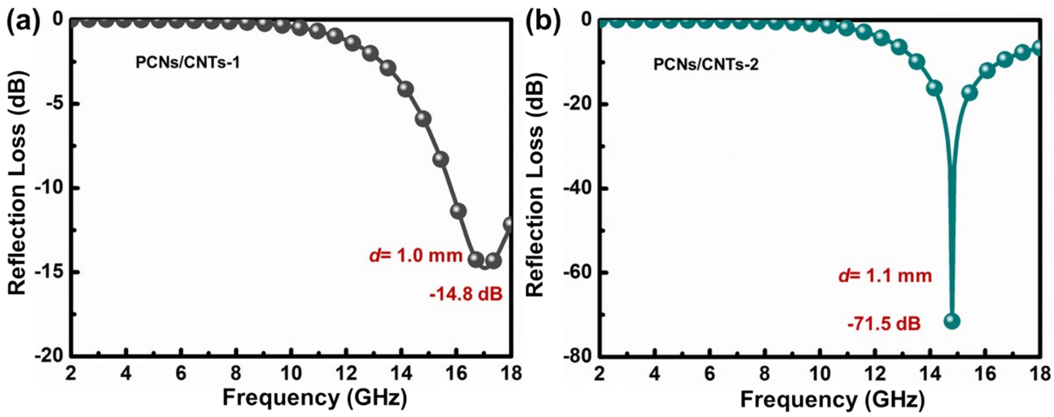

Fig. S18 *RL* curves of PCNs/CNTs-1 (a) and PCNs/CNTs-2 (b) in the frequency range of 2.0-18.0 GHz.

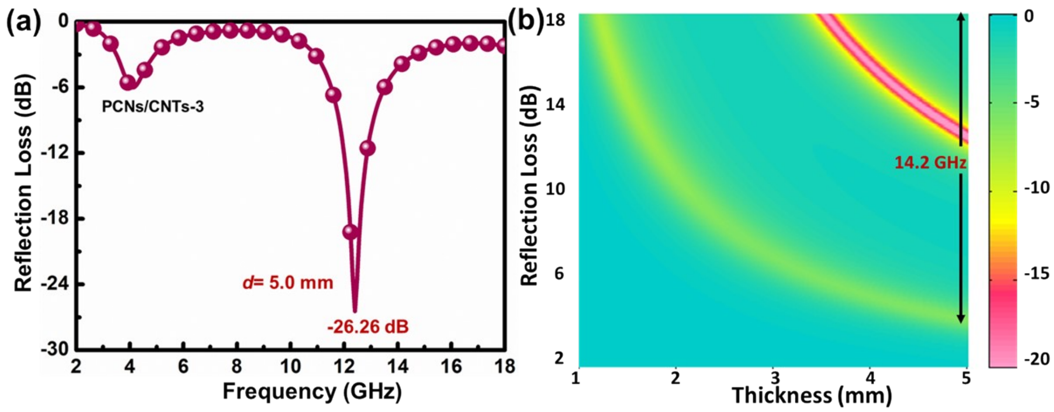

Fig. S19 *RL* curve (a) and planar *RL* map (b) of PCNs/CNTs-3 in the frequency range of 2.0-18.0 GHz.

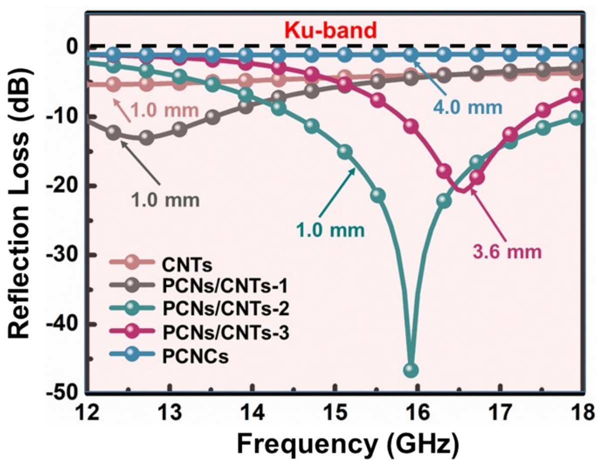

Fig. S20 Optimal *RL* curves in the Ku-band of CNTs, PCNs/CNTs-1, PCNs/CNTs-2, PCNs/CNTs-3, and PCNCs.

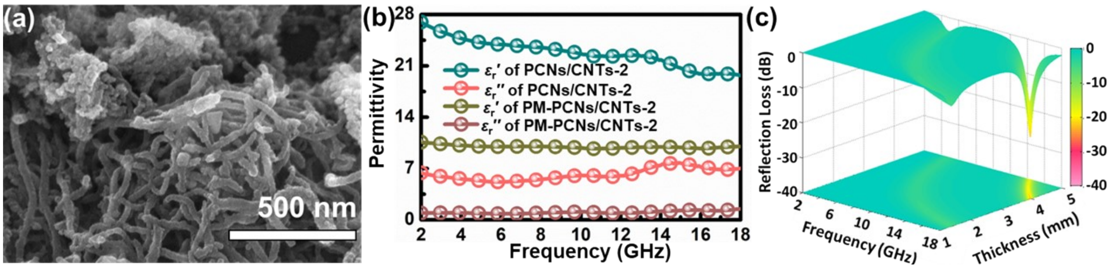

Fig. S21 SEM image of PCNs/CNTs-2 (a); The relative complex permittivity (b) of PCNs/CNTs-2 and PM-PCNCs/CNTs -2; *RL* maps of PM-PCNCs/CNTs-2 (c).

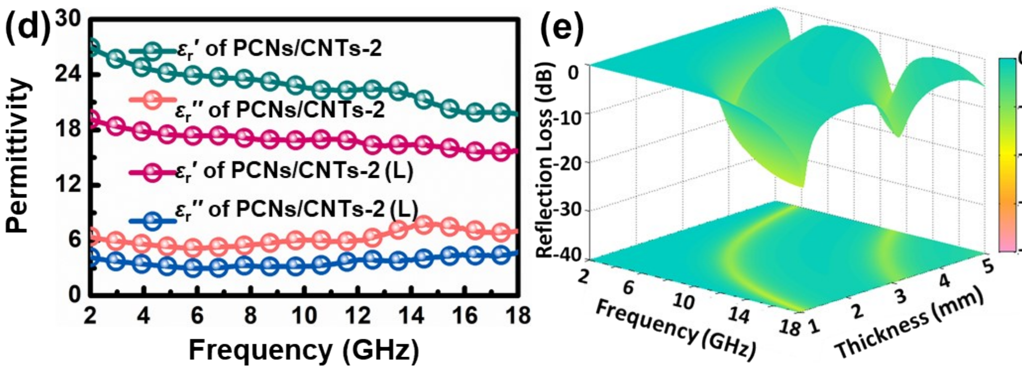

Fig. S22 The relative complex permittivity (a) of PCNs/CNTs -2 and PCNs/CNTs -2 (L); RL maps of PCNs/CNTs -2 (L) (b).